

Organic Electronics Circuitry for In Situ Real-Time Processing of Electrophysiological Signals

Anna De Salvo, Federico Rondelli, Michele Di Lauro,* Alice Tomassini, Pierpaolo Greco, Thomas Stieglitz, Luciano Fadiga, and Fabio Biscarini

The next generation of brain–machine interfaces are envisioned to couple signal transduction, filtering, and sorting on board with minimum power consumption and maximum bio-integrability. These functional needs shall be mandatorily met in order to design efficient closed-loop brain–machine interfaces aimed at treating and monitoring various disorders of the central and peripheral nervous system. Here, the pivotal role is highlighted that organic bioelectronics may have in the contextual development of all these three *desiderata*, by demonstrating a modular organic-electronics circuit toward real-time signal filtering. The inherent filtering capabilities of electrolyte-gated organic transistor are tuned via adjustment of operational conditions and benchmarked in an electromyography experiment. Additionally, a whole-organic signal processing circuitry is presented, coupling such transistors with ad hoc designed organic passive components. This provides the possibility to sort complex signals into their constitutive frequency components in real time, thereby delineating innovative strategies to devise organic-based functional building-blocks for brain–machine interfaces.

1. Introduction

Animals and humans can be regarded as “machines” living in a complex environment that continuously overloads their senses with information that may be crucial to establish social bonds or to decide the next course of action. Therefore, the brain must constantly select the most relevant information to build and update internal models that are used to predict what will happen next. This complexity leads to the transformation of endogenous and exogenous signals into a sophisticated mixture of electrical and chemical signal patterns that constitute the main currency upon which computations are run by the brain itself. In an extreme reductionist sense, this translates into the ability to select and process only specific frequency-encoded events while ignoring stimuli falling outside relevant bandwidths of information

content. While this task is performed in the brain by algorithms and machinery perfected over eras of evolutionary processes, replicating it with man-made information technology necessitates power-consuming off-line signal processing strategies and architectures, inevitably posing technological, energetic, and computational hurdles. Such effort, namely the mimicking of brain signal processing capabilities, is strongly intertwined with the need of understanding brain functioning mechanisms. This task requires the development of efficient brain–machine interfaces, with the ultimate goal of establishing a bidirectional communication between the brain and electronic devices.^[1,2]


The integration between biological environment and electronics is still an open challenge in disparate research and technology fields, encompassing bio-photovoltaics devices,^[3,4] sensors,^[5,6] organ-on-chip,^[7] implantable electronic devices^[8–10] and multi-functional neuromorphic components and circuits.^[11,12] The latter, especially when they are built on organic semiconductive moieties, are strongly gathering interest since, besides being promptly interfaced with living matter, they are capable of mimicking the primary signal-processing features of biological computing units and networks, like neurons and synapses, with a few components.^[13–15] This unprecedented capability arises from the matching between the response timescales of the organic devices and the timescales of biological processes, being both in the 1–1000 ms range.^[16] Notably, the characteristic

A. De Salvo, F. Rondelli, P. Greco, L. Fadiga
 Sezione di Fisiologia
 Dipartimento di Neuroscienze e Riabilitazione
 Università di Ferrara
 Via Fossato di Mortara 17–19, Ferrara 44121, Italy

A. De Salvo, F. Rondelli, M. Di Lauro, A. Tomassini, L. Fadiga, F. Biscarini
 Center for Translational Neurophysiology of Speech and Communication
 Fondazione Istituto Italiano di Tecnologia (IIT-CTNSC)
 Via Fossato di Mortara 17-19, Ferrara 44121, Italy
 E-mail: michele.dilauro@iit.it

T. Stieglitz
 Department of Microsystems Engineering (IMTEK)
 University of Freiburg
 79110 Freiburg, Germany

F. Biscarini
 Dipartimento di Scienze della Vita
 Università di Modena e Reggio Emilia
 Via Campi 103, Modena 41125, Italy

 The ORCID identification number(s) for the author(s) of this article can be found under <https://doi.org/10.1002/admi.202300583>

© 2023 The Authors. Advanced Materials Interfaces published by Wiley-VCH GmbH. This is an open access article under the terms of the Creative Commons Attribution License, which permits use, distribution and reproduction in any medium, provided the original work is properly cited.

DOI: 10.1002/admi.202300583

timescales of conventional electronics are in the ns– μ s range. The relevant timescale matching constitutes a key-enabling feature of organic electronics as eligible technological platform toward the ambitious goal of interfacing, understanding, and emulating human brain. This implies that the brain–machine interface (BMI) must perform brain signal transduction, amplification, and sorting.

Concerning signal transduction, recent research has been focused on non-invasive micro-epicortical (μ -ECoG) electrode arrays which are ultra-conformable to the brain cortex and provide high spatial resolution. On the other hand, miniaturization of epicortical electrodes results in a decreased signal-to-noise-ratio (SNR) with respect to large electrodes that transduce local-field potentials rather than single neuron spiking.^[17] A possible route to tackle this crucial shortcoming, targets minimization of interfacial impedance by either integrating organic (semi-)conductive coatings or by means of topographic surface engineering.^[18–20] These strategies enabled collection of neural spiking data directly from the brain cortex, broadening the clinical applicability of μ -ECoG and potentially overcoming the drawbacks of invasive intracortical electrodes, which are the golden standard for the transduction of single neuron activity. Despite the high significance of such approaches, SNR maximization remains an open issue in non- or mildly-invasive electrophysiology, aiming at high-quality and high-significance recording.

Toward this aim, there has been a sizable effort concerning the integration of in situ amplifiers in miniaturized BMIs. A distinctive approach by organic bioelectronics is to replace micro-electrodes with low-voltage/high-gain organic electronic transistors, that act as transconductance-based amplifiers. Most of the demonstrated work was performed with electrolyte-gated organic transistors (EGOTs), which also enable operation within a safe electrochemical window.^[9,21–24]

Interestingly, this periodizing advancements in signal transduction and amplification are not mirrored by a comparable counterpart focused on signal sorting. To date the transduced (and possibly amplified) signal is transferred without any further treatment to ex situ computing units, which are deputed to perform off-line data analysis, identifying relevant pathophysiological spectral ranges, detecting and removing artifacts, and classifying diagnostic patterns. This signal treatment is often manually driven by operators, and is time- and power-consuming, thereby strongly hampering the implementation of closed-loop, operator-independent, theranostic BMIs.

This work aims at providing a solution to these shortcomings, by presenting an organic flexible architecture for real-time signal sorting, prone to miniaturization and integration in BMIs, and specifically designed to be coupled to EGOT-based in situ amplifiers. The proposed technology makes advantage of organic analogs of passive circuit elements, namely organic resistors and electrolyte-organic capacitors, as building blocks for low- and high-pass passive filters to be coupled to EGOTs. Its signal sorting capabilities, as well as the inherent filtering features of EGOT, are herein presented and benchmarked against digitally generated model signals of increasing complexity, starting from “monochromatic” sinusoidal waves up to audio traces, and applied to achieve real-time filtering of human electrophysiological data, here specifically electromyographic (EMG) signals.

2. Results and Discussion

2.1. Organic Building Blocks

The choice of materials to implement the proposed signal sorting architecture is oriented to achieve prompt translatability, using only polyimide substrates, gold leads and poly(3,4-ethylenedioxythiophene) polystyrene sulfonate as organic resistor, as semi-conductive channel and gate electrode material in EGOTs and as interfacial layer in organic electrolyte capacitors (Figure 1a). Application-specific fabrication details are provided in the Experimental section. Passive low-pass (Figure 1b) and high-pass (Figure 1d) filters are built by connecting in series an organic electrolyte capacitor and an organic resistor, and connecting to ground the capacitor or the resistor, respectively. In this work, organic low-pass filters feature 6 Ω resistance and 295 μ F capacitor, while organic high-pass filters are built on 14 Ω resistance and 220 μ F capacitor. The input voltage, V_{IN} , is supplied at the non-grounded terminal of the series composed by the organic resistor and the organic electrolyte capacitor and the output voltage – termed V_L for the low-pass filter and V_H for the high-pass one – is collected at the shared node. The frequency profiles of organic filters are evaluated in response to monochromatic sinusoidal V_{IN} waves with peak-to-peak amplitude of 200 mV and frequency values ranging from 1 Hz to 1 kHz. Figure 1c,e shows the responses of low- and high-pass filters, respectively, in the form of Bode plots obtained calculating the gain of low-pass filters, $gain_{LP} = 20 \log_{10}(V_L/V_{in})$ and the gain of the high-pass filter, $gain_{HP} = 20 \log_{10}(V_H/V_{in})$. Cut-off frequencies, f_c , are estimated as the frequency values for which $gain_{LP} = -3$ dB for low-pass filters and $gain_{HP} = -19$ dB for high-pass ones (i.e., 3 dB less than the maximum $gain_{HP} = -16$ dB value achieved in the investigated frequency range). The resulting cut-off frequencies are $f_c \approx 5$ Hz for the proposed organic low-pass filters and $f_c \approx 30$ Hz for the high-pass ones, with slopes equal to -6 dB per decade and 9 dB per decade, respectively.

Interestingly, the use of organic analogs of passive circuit elements causes two main effects with respect to inorganic solid-state counterparts, namely a red-shift of f_c with respect to theoretically expected values (both for high- and low-pass filters) and a substantially negative gain (around -16 dB) of the passed high-frequency band in the case of high-pass filters. Both these effects arise from the fact that, here, an electrolyte compartment is used as a capacitive element in RC filters. If, on the one hand, this enables the engineering of flexible architectures and the exploitation of the high equivalent capacitance values and of the fine tunability of a PEDOT/PSS-electrolyte interface,^[25] on the other it brings into play substantial deviations from ideal response, which should be taken into account. The main deviation of the proposed electrolyte organic capacitor from an ideal one is that the former features a non-negligible resistance contributed by the electrolyte solution, R_S , which is in series with the equivalent capacitor of the electrical double layer, C_{DL} . It is well known that, for standard RC passive filters, Equations (1) and (2) hold, for high-pass and low-pass configurations, respectively.

$$\frac{V_{out}}{V_{in}} = \frac{Z_R}{Z_R + Z_C} \approx \frac{\omega RC}{\omega RC + 1} \quad (1)$$

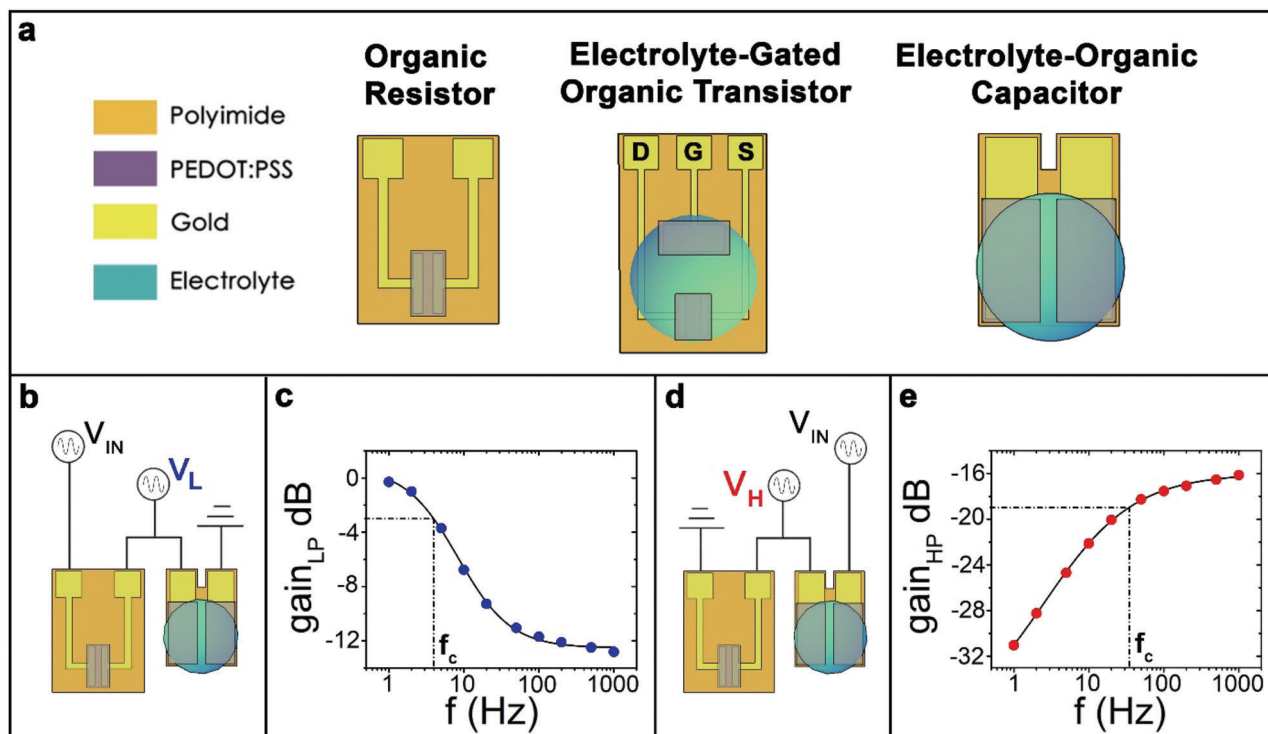


Figure 1. Organic building blocks. a) Schematic representation of the organic building blocks. b) Connection layout of the organic low-pass filter. c) Frequency profile of a representative organic low-pass filter, horizontal dashed black line intersects y-axis at -3 dB with respect to the maximum value, meanwhile vertical dashed black line intersects x-axis at the cut-off frequency value. d) Connection layout of the organic high-pass filter. e) Frequency profile of a representative organic high-pass filter, horizontal dashed black line intersects y-axis at -3 dB with respect to the maximum value, meanwhile vertical dashed black line intersects x-axis at the cut-off frequency value.

$$\frac{V_{out}}{V_{in}} = \frac{Z_C}{Z_R + Z_C} \approx \frac{1}{\omega RC + 1} \quad (2)$$

where Z_C and Z_R are the impedances of the resistor and of the capacitor, ω is the angular frequency of the input wave, $\omega = 2\pi\nu$, R is the resistance of the resistor, and C is the capacitance of the capacitor. The attenuation effect of R_S , observed solely in high-pass organic filters, is manifest by re-casting Equation (1) into Equation (3):

$$\frac{V_{out}}{V_{in}} = \frac{\omega RC_{DL}}{\omega (R + R_S) C_{DL} + 1} \quad (3)$$

Despite following the expected trend of a high-pass filter, namely being 0-valued at null frequency and growing linearly with ω when $\omega(R + R_S)C_{DL} \ll 1$, the V_{out}/V_{in} ratio approaches $R/(R + R_S)$ at the limit of infinite frequency, which necessarily is smaller than one. The entity of this attenuation is indeed a measure of the solution resistance. In the proposed high-pass filter (Figure 1d,e), where $R = 14 \Omega$, the plateau at -16 dB corresponds to $\frac{R}{R+R_S} \approx 0.156$ leading to an estimated $R_S \approx 75 \Omega$, which is coherent with the structure of the proposed capacitive element of organic RC filters.

Conversely, for the low-pass filter, the addition of R_S into Equation (2) yields Equation (4):

$$\frac{V_{out}}{V_{in}} = \frac{1}{\omega (R + R_S) C_{DL} + 1} \quad (4)$$

which predicts the ideal behaviour of a low-pass filter (i.e., $\frac{V_{out}}{V_{in}} = 1$ at $\omega = 0$ and $\frac{V_{out}}{V_{in}} = 0$ at $\omega = \infty$).

The red-shift effect observed on the cut-off frequency, f_c , arises from the equality between Equations (1) and (3) or (2) and (4) which implies that the response of the ideal filter to the input wave with angular frequency ω_1 , is equal to the response of (real) organic filter to the input wave with angular frequency ω_2 . By assuming $C = C_{DL}$, it turns out:

$$\omega_2 = \frac{R}{R+R_S} \omega_1 \quad (5)$$

since $R/(R + R_S)$ is always less than 1, this means that ω_2 will be always lower than ω_1 , quantitatively accounting for the red-shift in terms of solution resistance.

2.2. Electrolyte-Gated Organic Transistor

In addition to passive filters, the third building block for the proposed basic sorting-platform is the electrolyte-gated organic

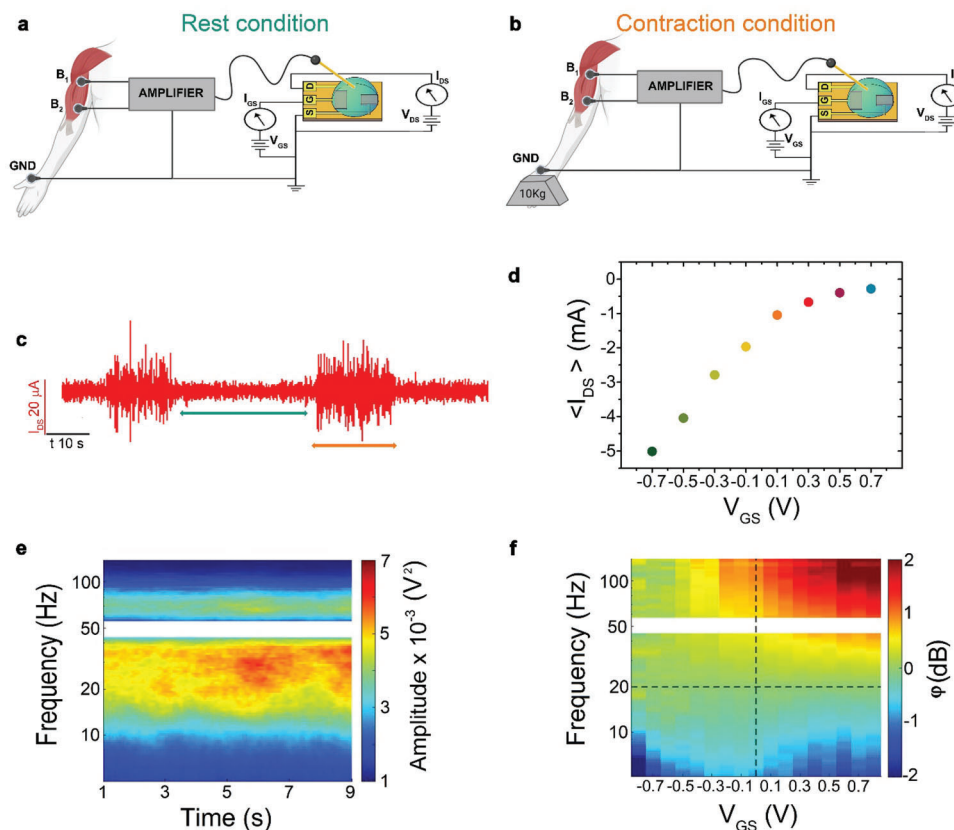


Figure 2. Filtering and sorting of electromyographic signal. a,b) Setup and the two different experimental condition for the EMG data acquisition. c) Recorded I_{DS} versus time trace highlighting the rest condition (green double headed arrow) and contraction condition (orange double headed arrow). d) Current DC-offset set by V_{GS} . Each point is the result of the average value of seven current EMGs traces versus the correspondent applied V_{GS} . e) Spectral content of V_{EMG} versus time EMG acquisition. f) Sorting efficiency map.

transistor. EGOTs were fabricated and characterized, as described in the Experimental Section. Briefly, EGOTs with aspect ratio (W/L) equal to 4 were used to implement the sorting platform and to record EMG signals. A PEDOT:PSS (Clevios PH1000, 5% v/v DMSO, 0.2% v/v GOPS) formulation, diluted ten times in MilliQ, was drop-cast in a well which exposed only the terminal portion of the source and drain leads (area = 0.8 mm × 0.9 mm). A PEDOT:PSS planar gate was obtained by following the same protocol. EGOTs were characterized in common-source/common-ground configuration (Figure S1a, Supporting Information) by acquiring transfer curves (Figure S1b, Supporting Information) and evaluating their bandwidth. This is done by applying monochromatic sinusoidal waves, at different DC offset values, at the gate electrode while recording the channel current (Figure S1b,d, Supporting Information), as described in the Experimental Section. Organic transistors generally act as low-pass filter, and their frequency band can be modulated not only acting on the device geometrical parameters^[23,26–28] but also varying the gate potential. Thus, increasing the density of mobile charges in the channel induces a slight shift of the cut-off frequency from higher to lower values (Figure S1d, Supporting Information).^[29] The frequency responses of the presented EGOTs show the expected trend, with a low-pass behavior and a gain set by the gate potential which also shows a minor influence on the cut-off frequency, especially for positive values. The gate DC-offset sets the

device cut-off frequency and its (quasi-static) transconductance, g_m , value, i.e., the EGOT potentiometric sensitivity in DC operation. Starting from negative to positive V_{GS} , the cut-off frequency of our devices blue shifts from 180 Hz to 220 Hz (Figure S1e, Supporting Information).

2.3. Transduction and Sorting of Electrophysiological Measurements

To benchmark EGOT V_{GS} -driven signal filtering and sorting capabilities in real time in the context of electrophysiological acquisitions, EGOTs were integrated in the processing chain of an EMG data recording session. Namely, we quantified the spectral content of muscle activity during steady isometric contraction at a moderate force level.

Figure 2a,b depicts the setup for EMG signal acquisition. Data are collected as described in the Experimental Section. Briefly, EMG signals (V_{EMG} versus time, Figure S2, Supporting Information) from the biceps brachii (acting as the prime mover in the current setting) were acquired during isometric contraction required to statically hold a 10 kg weight on the hand for 10 s; EGOT-mediated EMGs are collected as I_{DS} versus time traces. **Figure 3c** highlights the differences between rest and contraction (weight holding) conditions. As already mentioned, V_{GS} sets the

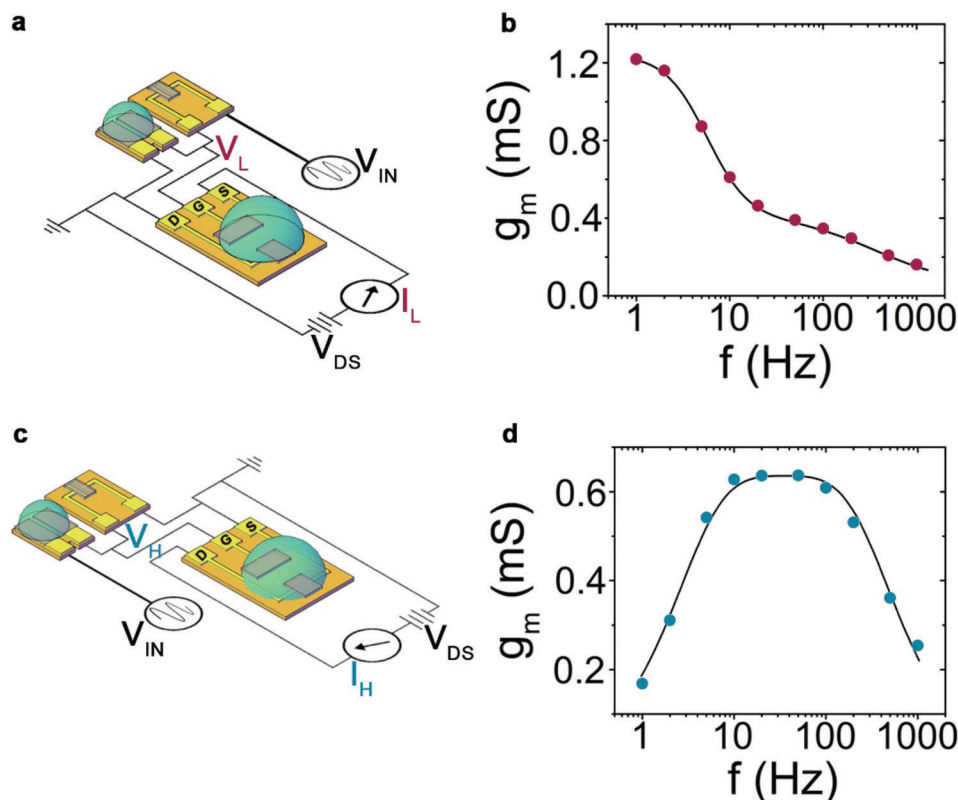


Figure 3. Coupling EGOTs with organic RC filters. a) Connection layout of the organic low-pass filter paired with EGOT. b) g_m versus frequency profile of the configuration in (a), black solid line is a double-boltzmann fit of the data, intended as a guide for the eye. c) Connection layouts of the band-pass filter, achieved pairing the EGOT with the organic high-pass filter. d) g_m versus frequency profile of the configuration in (c), black solid line is an inverse polynomial fit of the data, intended as a guide for the eye.

current DC-offset,^[11,29] as shown in Figure 2d, which reports the average value of current EMGs versus the correspondent applied V_{GS} . The $\langle I_{DS} \rangle$ versus V_{GS} profile closely mirrors EGOT transfer characteristics (see Figure S1b, Supporting Information). Each $\langle I_{DS} \rangle$ value is averaged over time and over trials between seven I_{DS} versus time traces acquired for each applied V_{GS} , see (Figure S3, Supporting Information). The spectral content of V_{EMG} versus time EMG acquisition is reported in Figure 3e. The spectral amplitude is not affected by the gate voltage, as shown by the individual spectral amplitude versus time EMG acquisition for each V_{GS} applied in Figure S4 (Supporting Information). Spectrogram (Figure 3e) shows, as expected, that the EMG spectral content is mainly concentrated between 10 and 100 Hz, regardless of V_{GS} . Muscle activity that is spectrally confined in the beta-band (≈ 15 –30 Hz) is of particular physiological relevance because it most likely has a central neurogenic origin, contributing a major component of the descending neural drive to the spinal motor neuron pool,^[30–32] and could function as a useful control signal in human-machine interfaces and motor augmentation platforms.^[33] Therefore, we focused on the relative spectral amplitude of muscle activity within the beta-band (centered at 20 Hz) with respect to both lower- and higher frequency content.

The transduction efficiency of EGOTs can be expressed by the index Ψ , corresponding to the ratio between the spectral amplitudes of I_{DS} versus time traces and that of V_{EMG} voltage, for each investigated frequency band and V_{GS} value. Ψ versus f versus V_{GS}

spectrogram is reported in Figure S5 (Supporting Information), and shows an analogous trend with respect to that observed for transconductance in Figure 2d.

Defining φ as the ratio between the Ψ value in the 19–21 Hz range (i.e., Ψ_{20}), and the Ψ value at each considered frequency band (i.e., Ψ_{fb}), expressing this ratio in dB as described in Experimental Section and plotting it against V_{GS} and frequency, it is possible to obtain a sorting efficiency map, Figure 2f. The effect of V_{GS} in evidencing one frequency band of interest (here 19–21 Hz) with respect to all the other spectral components can be quantitatively expressed by φ . On this premises, the gate voltage acts as a frequency-specific selector of transduction efficiency. Figure 2f provides a map of operational conditions for EGOT-transduced EMG, expressing which V_{GS} value is most suitable to evidence the 19–21 Hz band with respect to other spectral components (φ voltage and current map are reported in Figures S6 and S7 in the Supporting Information). In detail, for electrophysiological evaluations which could benefit from relative enhancing of beta-band activity and attenuation of higher-frequency components, positive V_{GS} should be applied, as testified by the strongly positive φ values in the top-right corner of Figure 2f, which indicate a strong predominance of the 19–21 Hz with respect to higher frequencies. This gain with respect to high-frequency spectral content is lost at negative V_{GS} (top-left corner of Figure 2f). On the other hand, to increase the transduction efficiency at 20 Hz with respect to the transduction efficiency of lower spectral components,

which would be naturally boosted by EGOTs, Figure 2f shows that EMG evaluations should be carried out with V_{GS} around 0 V (bottom center region of Figure 2f). Additionally, the sorting efficiency map in Figure 2f turns out to be a valuable tool also for applications that demand frequency-invariant transduction efficiency, by identifying the proper V_{GS} regime ($V_{GS} \approx -0.4$ V, $\varphi \approx 0$ for all the investigated frequency bands).

2.4. Coupling EGOTs with Organic RC Filters

As already mentioned, EGOTs act as low pass filters, albeit with rather wide bandwidth. This means that, every time EGOTs are used for transduction, the entire information content which falls in the EGOT passing band is collected and amplified and this ultimately results in poor frequency-selectivity. As discussed, frequency band selectivity is highly desirable in closed-loop BMIs since it would limit transduction to specific pathologically relevant events, which may serve as triggers for the real-time loco-regional treatment, be it chemical or electrical.^[34–36] This would result in improved compliance and durability and in the minimization of side effects due to overuse. Bandwidth tuning in EGOTs is usually addressed by acting on geometrical device parameters. On the one hand, it is possible to redshift EGOT's cut-off frequency by engineering large area devices,^[37] at the price of losing some spatial resolution when aiming at their translation to epicortical arrays. Conversely, it is possible to widen their frequency range (i.e., to blue-shift their cut-off frequency) by miniaturization,^[26,27] at the price of significantly lowering the transconductance. Both these approaches fail in yielding band-selective devices with both high spatial resolution and good amplification capability. At this purpose, by making advantage of the inherent filtering properties of EGOTs and coupling them with organic passive building blocks, it is possible to tighten the bandwidth toward lower frequencies or to implement band-pass filters. The first scenario is achieved by coupling the low-pass filter with an EGOT (Figure 3a). Conversely, the second one arises from the coupling between an EGOT and a high-pass filter (Figure 3c). In these configurations, the filters' output voltages, termed V_L and V_H , are used as input gate voltages for the EGOTs, keeping a constant channel bias, $V_{DS} = -0.7$ V. The resulting channel currents are termed I_L and I_H , for the configurations in Figure 4a,c, respectively. Transconductance versus frequency profiles are obtained by dividing the amplitudes of I_L and I_H by the amplitude of the input voltages. The configuration in Figure 4a exhibits low-pass behavior with a cut-off frequency as low as 5 Hz (Figure 3b), while the configuration in Figure 4b exhibits a band-pass profile from 5 Hz to 90 Hz (Figure 3d). These two independent architectures can be paired to foster a platform to sort and amplify a common V_{IN} in two differently factorized output signals, as discussed in the next section.

2.5. Sorting Circuitry

In Figure 4a the sorting platform architecture sketch is reported. A common V_{IN} is driven through the filter inputs and the resulting V_L and V_H are connected to two EGOTs gate electrodes. The channel currents are recorded by fixing V_{DS} equal to -0.7 V, as

discussed in the Experimental Section. To validate our architecture a first characterization was performed by applying sinusoidal waves with a peak-to-peak amplitude of 200 mV and frequencies spanning from 1 to 1000 Hz as common input signals, while collecting I_L and I_H .

The current amplitude versus frequency trends are reported in Figure 4c, highlighting the sorting platform frequency-response, closely mirroring the transconductance trends in Figure 4. After validating its operation with monochromatic waves, a sweep wave with 200 mV peak-to-peak amplitude and frequency interval from 1 to 200 Hz was used as input signal. The I_L and I_H currents versus time are reported in Figure 4b (bottom panel), showing that the designed basic circuit enables to discriminate both in amplitude and in frequency the output responses in real-time.

To benchmark the sorting efficiency of the proposed architecture against a more complex signal, a pre-recorded in vivo somatosensory evoked potential (SEP), which is a well-defined potential modulation in the rat barrel cortex, is digitalized,^[38,39] Figure 4d, and driven (see Experimental Section) as input signal. In a translational perspective, we want to test its sensitivity in discriminate some of the relevant frequency bands that are usually evaluated in SEP characterization: α (5 Hz – 15 Hz), β (15 Hz – 30 Hz), low γ , γ_L (30 Hz– 80 Hz), and high γ , γ_H (80 Hz – 150 Hz), band.^[9,40] Digitalised SEP amplitude was increased to 200mV_{pp} to use it as a V_{IN} model signal. I_L and I_H are recorded by keeping drain-source voltage at -0.7 V.

Defining η as the percentage of total power in the selected frequency interval, the analysis of the frequency content in relevant electrophysiological bands was performed, as discussed in the Experimental Section. Briefly, η_L (η_H) is evaluated as the ratio between the power of a specific frequency band in the I_L (I_H) versus time trace and the broadband power of the same trace. Figure 4e reports the values of η_L and η_H versus the frequency bands. Even with complex event related signals, the sorting architecture successfully discriminates its different frequency domains. In particular, the low-pass branch of this architecture selects α and β frequency bands, as testified by the significantly higher values of η_L with respect to η_H in these frequency bands. Conversely, frequencies higher than 30 Hz are preferentially transmitted by the band-pass branch (i.e., $\eta_H > \eta_L$ for low-gamma activity). In the high-gamma frequency range there is a loss in transduction efficiency for both branches, since the EGOT implemented in this design has a cut-off frequency of roughly 120 Hz and, as a consequence, the gain of both branches drops at high frequencies. To further mark the frequency-related gain-switch between the sorting platform branches, it is possible to estimate a sorting factor, reported versus frequency in Figure 4f. The sorting factor is computed by dividing the I_L and I_H output signals in 13 equally spaced intervals, as described in the Experimental Section, and calculating the power of each frequency interval. The ratio between the I_L power in a specific frequency band and the I_H power in the same frequency band results in the sorting factor, which is a quantitative estimate of the preferential routing of that frequency among the two branches of the sorting architecture. If, for a given frequency interval the sorting factor exceeds unity, the signal content in that frequency interval will be preferentially transduced as I_L . Conversely, frequency intervals that yield sorting factors minor than one will be preferentially transduced as I_H . In the proposed architecture, the sorting factor equals one in

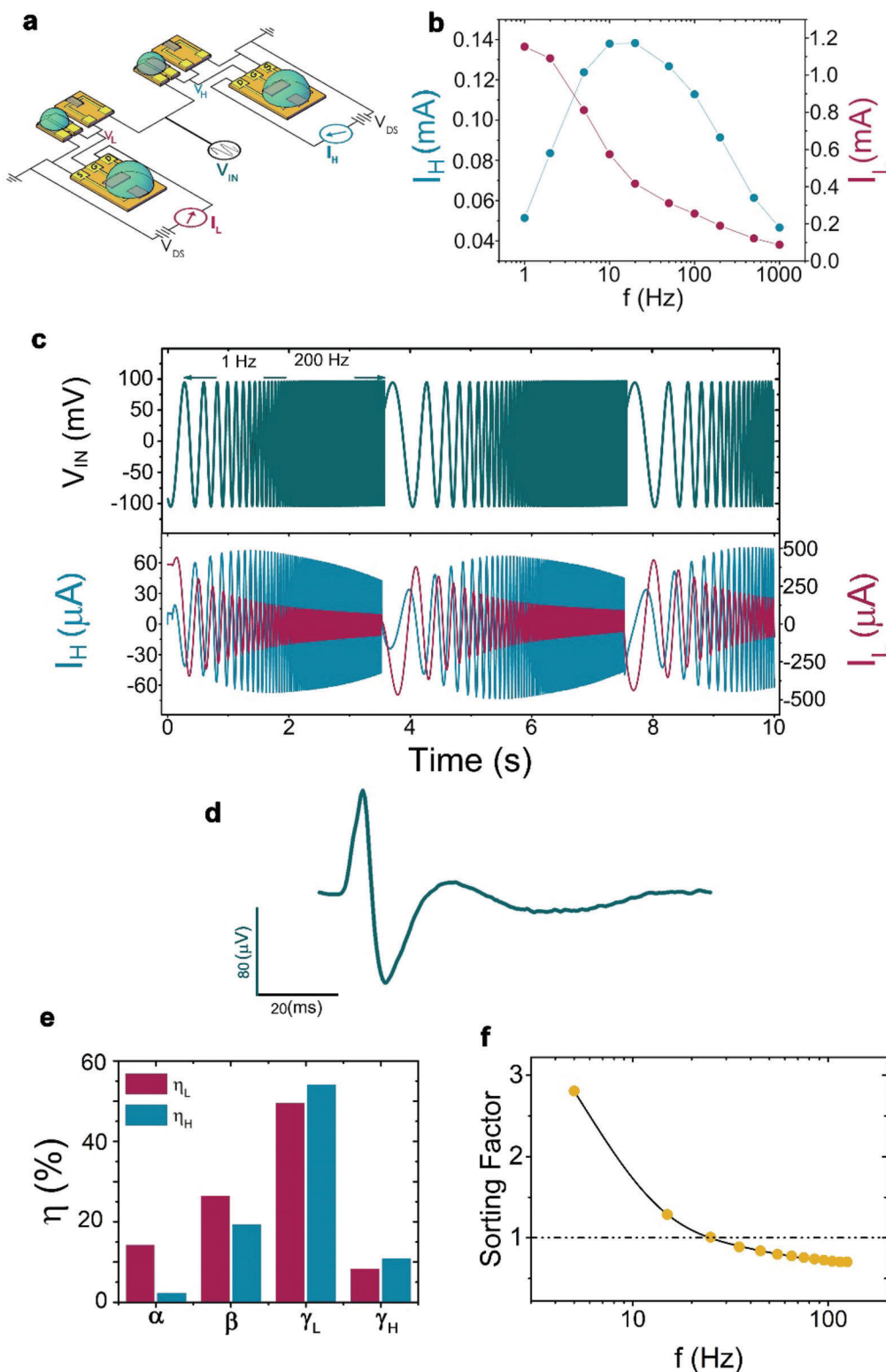


Figure 4. Sorting platform. a) Sorting platform connection layout. b) Sweep wave exploited as V_{IN} for the sorting platform (top panel) and I_H and I_L current output (bottom panel). c) The frequency response of I_H and I_L determined by supplying the sorting platform with a monochromatic sinusoidal wave. d) Pre-recorded in vivo somatosensory evoked potential used as input for the sorting platform. e) percentage of total power in frequency electro-physiological interval α 5–15 Hz; β 15–30 Hz; low-gamma γ_L 30–80 Hz; high-gamma γ_H 80–150 Hz. f) Sorting factor. Dash-dot line highlights the unitary gain for the sorting platform. The intersection between this line and the experimental point sets the frequency turning point at 28 Hz, black solid line is a two-phase exponential decay fit of the data, intended as a guide for the eye.

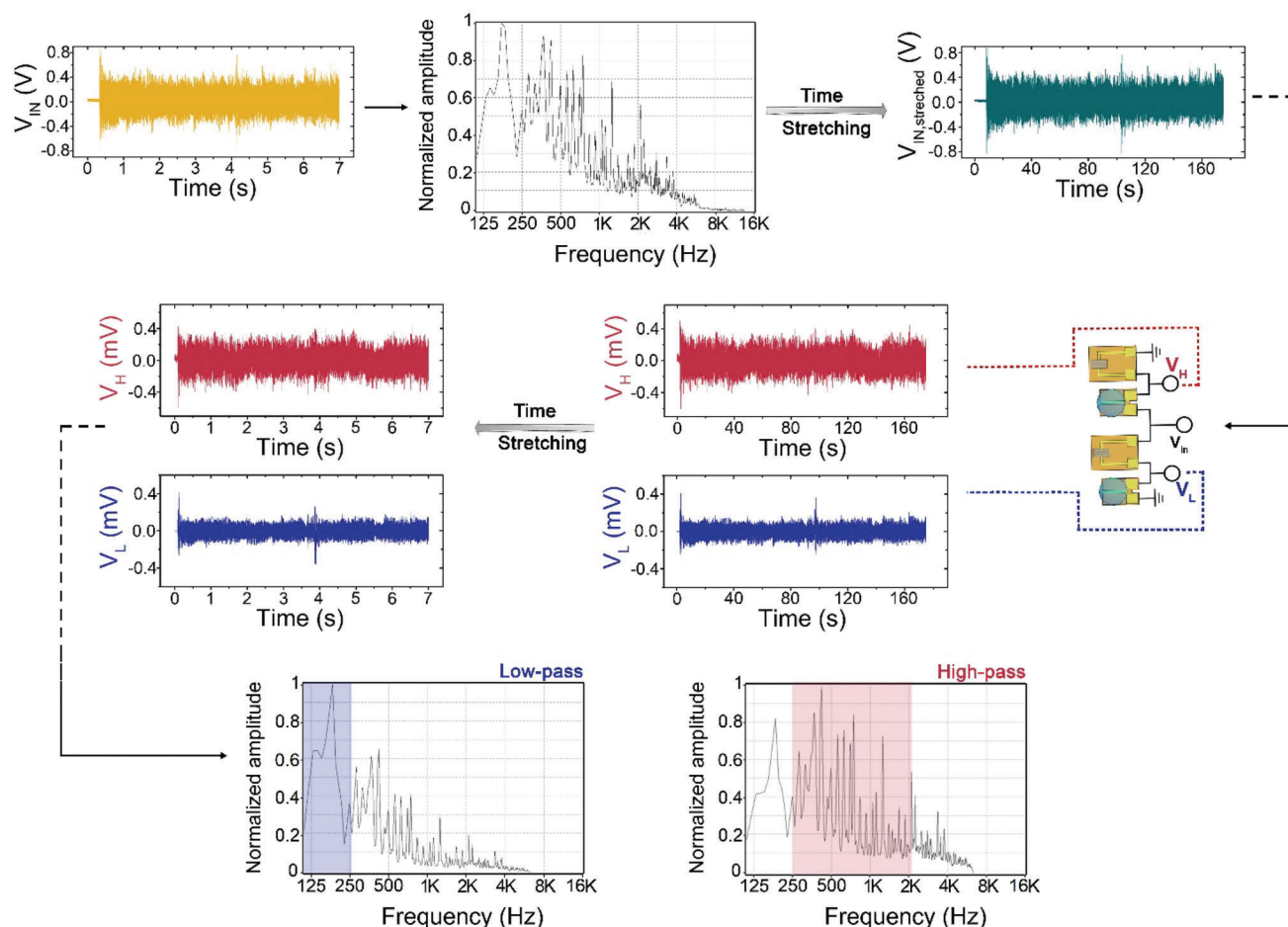


Figure 5. Audio trace transduction chain. From left to right: seven seconds of the audio trace are used as input signal. Unfiltered signal spectrum is evaluated. The voltage trace is then time-stretched such as its frequency content falls in the operational range of the proposed filters. The stretched signal, which lasts 175 s (top right), is used as V_{IN} for the paired filters; V_L and V_H are recorded. A re-stretching of the signals back to the original duration ensures audio reproducibility. V_L and V_H traces (second row, on the left) are used to evaluate low- and high-passed signal spectra (bottom panels). In the low- and high-passed spectra, the blue and the red box highlight the spectral region of maximum relevance.

the 20–25 Hz interval, Figure 4f, meaning that spectral content in this frequency interval remains unsorted and can be found with equal power in I_L and in I_H .

2.6. Signal Factorization and Independent Routing with Organic RC Filters

As a last example of the versatility of our material/device platform, we show the design and operation of a standalone sorting circuitry by pairing RC organic filters. We demonstrate it on the equalization of an analog audio signal. Audio signals were chosen as archetypes of frequency-encoded information, with relevant spectral content across a wide frequency range, namely between 20 Hz and 20 kHz. Since our architecture is tailored to operate in the 0.1–1500 Hz range relevant to electrophysiological signals, we had to adopt an out-of-the-box modification of the input signal to adapt it to the doable processing window of the circuitry. For this, by time-stretching an audio trace of a factor 25, as described in the Experimental Section, we bring it in the desired operational

range, while preserving its information content. In Figure 5 the signal processing chain of an audio sorting experiment is shown. A common audio signal input to the paired organic RC filters is split in real time into two differently equalized output signals. In detail, an audio track, namely 7 seconds of the introduction of “Sweet Child of Mine” by Guns ‘n Roses, is acquired as voltage versus time, as discussed in the Experimental Section. The voltage track is used as V_{IN} for the filter architecture and V_L and V_H are collected. Figure 5 (top center) depicts the spectra of the untreated input signal, the low-passed and the high-passed signal spectra are shown in Figure 5 (bottom). By time stretching these signals of a factor 1/25 it is possible to hear the different equalization of the two branches, their related audio files can be downloaded as Audio S1 and Audio S2 in the Supporting Information. From the spectra, it is possible to notice how the normalized amplitude of the low-pass and high-pass spectra strongly differ in terms of frequency contribution. A major frequency content between 120 and 250 Hz can be observed in the low-passed spectrum with respect to the high-passed one, in which the dominant spectral contributions are above 250 Hz.

3. Conclusion

The ability to separate and independently route frequency-encoded information from a complex signal, as is typical in biological environments, may be essential for real-time monitoring of such activities. This task, which encompasses transduction, amplification, and sorting of the acquired signals, will enable their use as discrimination tools for pathophysiological pattern recognition. This work presents the possibility to merge the well-known EGOTs filtering and amplification capabilities, tested and verified at the benchside and with electromyographic signals, with an organic flexible architecture for real-time signal sorting that is prone to downsizing and integration in BMIs. Although it is specifically designed to pair EGOT-based in situ amplifiers, the signal sorting architecture can also be coupled with electrode technology, offering a novel operational paradigm for real-time data treatment. This possibility to segment information in an *in operando* condition is oriented to translation in bio-integrable circuitry. At this purpose, organic filters and EGOTs were implemented on polyimide and using PEDOT:PSS as active moiety, hence exploiting some of the most used materials in organic bioelectronics and extending the available toolset for direct integration of filtering and sorting circuitry in ultra-conformable BMIs, which constitutes a major advantage of this approach with respect to classical *ex situ* filtering strategies.

4. Experimental Section

Materials: Formulation for PEDOT:PSS drop-casting had been achieved by adding 5% v/v dimethylsulfoxide (DMSO, Merck) and 0.2% (3-glycidyloxypropyl)trimethoxysilane (GOPS, Merck) to commercial Clevis PH1000 (Heraeus). Sodium poly-styrene sulfonate (NaPSS, Merck) and 3,4-ethylenedioxythiophene (EDOT, Merck) were used for electrodeposition of PEDOT/PSS. Kapton-supported gold electrodes were achieved by metallization (10 nm Nickel Chromium adhesive layer, 70 nm Au, Crevac – Creative Vakuumbeschichtung GmbH) of 50 μm thick Kapton (polyimide) sheets. Test patterns for EGOT fabrication were custom-designed and purchased from Phoenix PCB. Phosphate-buffered saline solution 1 M (Merck) had been used as electrolyte.

Electrolyte-Organic Capacitor: Two Au electrodes supported on the same Kapton sheet (active area of each electrode = 0.3 cm^2) were coated by means of potentiostatic electrodeposition of PEDOT/PSS (5s 0.2 V, then 0.8 V in charge limit control, up to the desired charge density), starting from an aqueous electrolyte containing 10 mM EDOT and 5 mg mL^{-1} NaPSS. Investigated charge densities were 83 and 166 mC cm^{-2} , which resulted in equivalent capacitance values of $220 \pm 10 \mu\text{F}$ and $295 \pm 18 \mu\text{F}$ at 100 Hz (measured by a precision LCR bridge, Thurlby Thandar Instruments) when exposed to the PBS electrolyte.

Organic Resistor: PEDOT:PSS formulation was diluted 1:2 with MilliQ H_2O and drop-cast between two Au electrodes of the test patterns designed for EGOT fabrication (0.5 μL on a 0.72 mm^2 area). Average resistance value was $2.9 \pm 0.2 \Omega$. Series combination of organic resistors were used to achieve the desired resistance values in the final signal sorting architecture.

Electrolyte-Gated Organic Transistor Fabrication: PEDOT:PSS formulation was diluted 1:10 with MilliQ H_2O and drop-cast in confined areas of test-patterns (0.5 μL on a 0.72 mm^2 area) to achieve a PEDOT:PSS semi-conductive channel ($W/L = 4$) and a co-planar PEDOT:PSS Gate electrode. Average thickness was 1 μm , as measured by atomic-force microscopy (XE7 AFM Park System, tapping mode)

Steady-State EGOT I-V Characterization: Steady-state electrical characterization was performed using a two-channel Keysight B2912A Source/Measure Unit and PBS electrolyte. For transfer characteristics,

gate voltage was linearly swept between -0.8 to 0.8 V by steps of 2 mV (scan rate = 100 mV s^{-1}) while drain voltage was kept constant at -0.7 V.

AC Characterization: An Agilent33220A arbitrary waveform generator was used as source of model signals. EGOT bandwidth was evaluated in a common source/common ground configuration by sourcing the gate potential with sinusoidal waves with amplitude equal to 200 mVpp and frequency ranging from 1 to 1000 Hz, recording I_{DS} values in time. Organic filters and sorting platform frequency-dependent profiles were characterized by applying at the V_{in} sinusoidal waves with amplitude equal to 200 mVpp and frequency ranging from 1 to 1000 Hz, recording the voltage output and the current output with a Source/Measurement Unit (SMU) (Keysight B2912A) in current mode and voltage mode, respectively. Pre-recorded somatosensory evoked potential was digitalized and stored in a Agilent33220A arbitrary waveform generator. This signal and a sweep signal with frequency ranging from 1 to 200 Hz were exploited as model signals to characterize the sorting platform filtering properties. Both signals were used as V_{in} with a final amplitude equal to 200 mVpp and the current output was recorded with a Source/Measurement Unit (SMU) (Keysight B2912A).

Audio Track Acquisition and Rescaling: Audio track was acquired as voltage versus time by directly connecting the mini-jack output of a laptop soundboard to the input of an Agilent Technologies DSO6012A oscilloscope 100 MHz 2GSa/s, sampling at 50 kHz. The collected track was reproduced using Matlab Audio Toolbox at a 25-times lower speed and used as V_{in} for the coupled organic filters. The output voltages were collected with a Source/Measurement Unit (SMU) (Keysight B2912A) in current-control mode at a sampling frequency equal to 500 Hz. The two filtered output voltages were played back at normal speed using Matlab Audio Toolbox.

EGOT-EMG Set-Up and Acquisition: Surface EMG signals were acquired by an Isolated Patient Amplifier System (Digitimer, D360) in terms of electromyographic voltage, V_{EMG} , which was notched at 50 Hz and amplified 100x by the acquisition system. The muscle of interest – i.e., the biceps brachii (short head) – was identified via standard palpation procedures, and Ag/AgCl electrodes ($\phi = 5$ mm) were placed on the muscle belly with an interelectrode distance of ≈ 5 cm. Upon the acquisition of electromyographic activity, V_{EMG} was contextually acquired by a Source/Measure unit (Agilent Technologies, B2912A) voltage and transmitted via a bathing needle-shaped electrode to the operational electrolyte of an EGOT (PBS 1 M). EGOT channel current, I_{DS} , was acquired by another Source/Measure unit, which sources constant $V_{\text{DS}} = -0.7$ V and V_{GS} ranging from -0.8 to 0.8 V with steps of 100 mV. All signals were acquired at 5000 Hz. Data were collected on a healthy subject (the co-author FR; male, age: 26 years). The subject was comfortably seated and held his right arm bent in a supine position with his elbow resting on a fixed support. Each recording was manually initiated by the experimenter after placing a 10-kg cast iron weight on the subject's right hand (ensuring that the hand was already stabilized after loading) and lasted for 10 s; at the end of the 10-s recording, the weight was removed from the hand and a short pause (≈ 1 min) was taken before starting the next recording. A total of 7 recordings were performed for each V_{GS} in a fully randomized order to exclude potential order effects, e.g., due to muscle fatigue.

Data Analysis: Data analysis and graphing had been performed with Origin 2016, Matlab (version 9.10, Mathworks, Natick, MA, USA) and the FieldTrip toolbox.^[41] Specifically, to examine the data in the time-frequency domain, the Matlab function spectrogram was used setting a window length of 100 samples and 90% of window overlap. Power Percentage was estimated by filtering the data with Matlab function *designfilt* in four frequency bands. For each filtered signal and for the broadband signal the power was estimated with matlab function *bandpower* and the power of each band-filtered dataset was divided by its broadband signal power. Sorting factor was estimated by exploiting Matlab function *bandpower* dividing the signals in 13 frequency band and subsequently calculating their ratio. Spectral analysis of the audio signals had been performed with Steinberg Cubase 5.0.

To quantify the spectral content of the EMG signals, conventional Fourier analysis was applied in combination with the multitaper method^[42] which allowed for increasing the signal-to-noise ratio and

controlling spectral smoothing. Before converting into the frequency domain, the I_{DS} versus time traces were high-pass filtered (cut-off: 0.1 Hz; two-pass Butterworth filter, third order for each pass) to remove the V_{GS} -dependent DC-offset. I_{DS} and V_{EMG} voltage (10-s time-series) were multiplied with a set of 39 orthogonal tapers (discrete prolate spheroidal sequences or Slepian functions) yielding 2-Hz spectral smoothing. The taper-specific Fourier-based amplitudes were estimated for 100 logarithmically (\log_{10}) spaced frequencies between 5 and 140 Hz, averaged over the tapers and then across the time-series ($n = 7$; see above) to derive the spectral amplitude for each V_{GS} . The transduction efficiency of EGOTs (Ψ) was calculated as the ratio between the spectral amplitudes of I_{DS} versus time traces and that of V_{EMG} voltage (for each frequency and V_{GS}). Finally, the ratio between Ψ values averaged between 19 and 21 Hz (Ψ_{20}) to all band-specific Ψ values (Ψ_{fb} ; computed by averaging Ψ values between two logarithmically increasing adjacent frequencies in the range 5–140 Hz) was calculated and converted to decibels for each V_{GS} as follows:

$$\varphi_{fb} = 10 \times \log_{10} \left(\frac{\Psi_{20}}{\Psi_{fb}} \right) \quad (6)$$

Time-frequency representations of V_{EMG} were obtained by applying the same analytic approach described above (i.e., Fourier with multitapering) on a shorter 1-s sliding window that was advanced over the data from 1 to 9 s in 50-ms steps. Spectral smoothing was set to 2 Hz (as for the 10-s time series analysis; see above) by multiplying each 1-s window with 3 orthogonal tapers.

Supporting Information

Supporting Information is available from the Wiley Online Library or from the author.

Acknowledgements

Research work leading to this publication was funded by IIT-Istituto Italiano di Tecnologia, University of Ferrara and University of Modena and Reggio Emilia (FAR2018 project e-MAP).

Conflict of Interest

The authors declare no conflict of interest.

Author Contributions

A.D.S. and F.R. contributed equally to this work.

Data Availability Statement

The data that support the findings of this study are available from the corresponding author upon reasonable request.

Keywords

electrolyte-gated organic transistors, organic bioelectronics, organic electronic filters, real-time signal processing, signal sorting

Received: July 7, 2023
Revised: August 13, 2023
Published online:

- [1] N. Even-Chen, D. G. Muratore, S. D. Stavisky, L. R. Hochberg, J. M. Henderson, B. Murmann, K. V. Shenoy, *Nat. Biomed. Eng.* **2020**, *4*, 984.
- [2] J. D. Kendall, S. Kumar, *Appl. Phys. Rev.* **2020**, *7*, 011305.
- [3] M. Di Lauro, S. Gatta, C. A. Bortolotti, V. Beni, V. Parkula, S. Drakopoulou, M. Giordani, M. Berto, F. Milano, T. Cramer, M. Murgia, A. Agostiano, G. M. Farinola, M. Trotta, F. Biscarini, *Adv. Electron. Mater.* **2020**, *6*, 1900888.
- [4] M. Di Lauro, G. Buscemi, M. Bianchi, A. De Salvo, M. Berto, S. Carli, G. M. Farinola, L. Fadiga, F. Biscarini, M. Trotta, *MRS Adv.* **2020**, *5*, 985.
- [5] M. Giordani, M. Sensi, M. Berto, M. Di Lauro, C. A. Bortolotti, H. L. Gomes, M. Zoli, F. Zerbetto, L. Fadiga, F. Biscarini, *Adv. Funct. Mater.* **2020**, *30*, 2002141.
- [6] H. H. Choudhry, D. H. Lee, A. Bag, N.-E. Lee, *Nat. Commun.* **2023**, *14*, 821.
- [7] G. A. Clarke, B. X. Hartse, A. E. Niaraki Asli, M. Taghavimehr, N. Hashemi, M. Abbasi Shirsavar, R. Montazami, N. Alimoradi, V. Nasirian, L. J. Ouedraogo, N. N. Hashemi, *Sensors* **2021**, *21*, 1367.
- [8] M. Vomero, M. F. Porto Cruz, E. Zucchini, F. Ciarpella, E. Delfino, S. Carli, C. Boehler, M. Asplund, D. Ricci, L. Fadiga, T. Stieglitz, *Biomaterials* **2020**, *255*, 120178.
- [9] M. Di Lauro, E. Zucchini, A. De Salvo, E. Delfino, M. Bianchi, M. Murgia, S. Carli, F. Biscarini, L. Fadiga, *Adv. Mater. Interfaces* **2022**, *9*, 2101798.
- [10] D. Khodagholy, J. N. Gelinias, Z. Zhao, M. Yeh, M. Long, J. D. Greenlee, W. Doyle, O. Devinsky, G. Buzsáki, *Sci. Adv.* **2016**, *2*, 1601027.
- [11] M. Di Lauro, A. De Salvo, G. C. Sebastianella, M. Bianchi, S. Carli, M. Murgia, L. Fadiga, F. Biscarini, *ACS Appl. Electron. Mater.* **2020**, *2*, 1849.
- [12] P. Gkoupidenis, N. Schaefer, B. Garlan, G. G. Malliaras, *Adv. Mater.* **2015**, *27*, 7176.
- [13] P. C. Harikesh, C.-Y. Yang, D. Tu, J. Y. Gerasimov, A. M. Dar, A. Armada-Moreira, M. Massetti, R. Kroon, D. Bliman, R. Olsson, E. Stavrinidou, M. Berggren, S. Fabiano, *Nat. Commun.* **2022**, *13*, 901.
- [14] P. Gkoupidenis, D. A. Koutsouras, G. G. Malliaras, *Nat. Commun.* **2017**, *8*, 15448.
- [15] P. C. Harikesh, C.-Y. Yang, H.-Y. Wu, S. Zhang, M. J. Donahue, A. S. Caravaca, J.-D. Huang, P. S. Olofsson, M. Berggren, D. Tu, S. Fabiano, *Nat. Mater.* **2023**, *22*, 242.
- [16] G. Buzsáki, C. A. Anastassiou, C. Koch, *Nat. Rev. Neurosci.* **2012**, *13*, 407.
- [17] A. R. Hassan, Z. Zhao, J. J. Ferrero, C. Cea, P. Jastrzebska-Perfect, J. Myers, P. Asman, N. F. Ince, G. McKhann, A. Viswanathan, S. A. Sheth, D. Khodagholy, J. N. Gelinias, *Adv. Sci.* **2022**, *9*, 2202306.
- [18] C. Boehler, F. Oberueber, S. Schlabach, T. Stieglitz, M. Asplund, *ACS Appl. Mater. Interfaces* **2017**, *9*, 189.
- [19] S. Carli, L. Lambertini, E. Zucchini, F. Ciarpella, A. Scarpellini, M. Prato, E. Castagnola, L. Fadiga, D. Ricci, *Sens. Actuators, B* **2018**, *271*, 280.
- [20] M. Bianchi, A. De Salvo, M. Asplund, S. Carli, M. Di Lauro, A. Schulze-Bonhage, T. Stieglitz, L. Fadiga, F. Biscarini, *Adv. Sci.* **2022**, *9*, 2104701.
- [21] C. Cea, G. D. Spyropoulos, P. Jastrzebska-Perfect, J. J. Ferrero, J. N. Gelinias, D. Khodagholy, *Nat. Mater.* **2020**, *19*, 679.
- [22] W. Lee, D. Kim, N. Matsuhisa, M. Nagase, M. Sekino, G. G. Malliaras, T. Yokota, T. Someya, *Proc. Natl. Acad. Sci. USA* **2017**, *114*, 10554.
- [23] D. Khodagholy, T. Doublet, P. Quilichini, M. Gurfinkel, P. Leleux, A. Ghestem, E. Ismailova, T. Hervé, S. Sanaur, C. Bernard, G. G. Malliaras, *Nat. Commun.* **2013**, *4*, 1575.
- [24] J. Rivnay, P. Leleux, M. Sessolo, D. Khodagholy, T. Hervé, M. Focci, G. G. Malliaras, *Adv. Mater.* **2013**, *25*, 7010.

- [25] K. Tybrandt, I. V. Zozoulenko, M. Berggren, *Sci. Adv.* **2017**, *3*, eaao3659.
- [26] J. E. Tyrrell, M. G. Boutelle, A. J. Campbell, *Adv. Funct. Mater.* **2021**, *31*, 2007086.
- [27] Y. Liang, F. Brings, V. Maybeck, S. Ingebrandt, B. Wolfrum, A. Pich, A. Offenhäusser, D. Mayer, *Adv. Funct. Mater.* **2019**, *29*, 1902085.
- [28] J. Rivnay, P. Leleux, M. Ferro, M. Sessolo, A. Williamson, D. A. Koutsouras, D. Khodagholy, M. Ramuz, X. Strakosas, R. M. Owens, C. Benar, J.-M. Badier, C. Bernard, G. G. Malliaras, *Sci. Adv.* **2015**, *1*, 1400251.
- [29] F. Rondelli, A. De Salvo, G. Calandra Sebastianella, M. Murgia, L. Fadiga, F. Biscarini, M. Di Lauro, *Neuromorphic Comput. Eng.* **2023**, *3*, 014004.
- [30] B. A. Conway, D. M. Halliday, S. F. Farmer, U. Shahani, P. Maas, A. I. Weir, J. R. Rosenberg, *J. Physiol.* **1995**, *489*, 917.
- [31] S. N. Baker, *Curr. Opin. Neurobiol.* **2007**, *17*, 649.
- [32] M. Bräcklein, D. Y. Barsakcioglu, A. Del Vecchio, J. Ibáñez, D. Farina, *J. Neurosci.* **2022**, *42*, 3611.
- [33] M. Bräcklein, J. Ibáñez, D. Y. Barsakcioglu, D. Farina, *J. Neural Eng.* **2021**, *18*, 016001.
- [34] M. Dümpelmann, *J. Neural Eng.* **2019**, *16*, 041001.
- [35] M. Amiri, H. Aghaeinia, H. R. Amindavar, *Biomed. Signal Process. Control* **2023**, *79*, 104022.
- [36] A. S. Widge, E. Licon, S. Zorowitz, A. Corse, A. R. Arulpragasam, J. A. Camprodon, C. Cusin, E. N. Eskandar, T. Deckersbach, D. D. Dougherty, *J. Neuropsychiatry Clin. Neurosci.* **2016**, *28*, 38.
- [37] J. T. Friedlein, R. R. McLeod, J. Rivnay, *Org. Electron.* **2018**, *63*, 398.
- [38] M. E. Diamond, M. von Heimendahl, P. M. Knutsen, D. Kleinfeld, E. Ahissar, *Nat. Rev. Neurosci.* **2008**, *9*, 601.
- [39] C. C. H. Petersen, *Neuron* **2007**, *56*, 339.
- [40] M. Vomero, E. Castagnola, F. Ciarpella, E. Maggiolini, N. Goshi, E. Zucchini, S. Carli, L. Fadiga, S. Kassegne, D. Ricci, *Sci. Rep.* **2017**, *7*, 40332.
- [41] R. Oostenveld, P. Fries, E. Maris, J.-M. Schoffelen, *Comput. Intell. Neurosci.* **2011**, *2011*, 156869.
- [42] D. B. Percival, A. T. Walden, in *Spectral Analysis for Physical Applications*, Cambridge University Press, Cambridge **1993**.